





Cite this: *Soft Matter*, 2020, **16**, 1866

## Escape dynamics of liquid droplets confined between soft interfaces: non-inertial coalescence cascades†

Maciej Chudak, <sup>a</sup> Jesse S. Kwaks,<sup>a</sup> Jacco H. Snoeijer<sup>ab</sup> and Anton A. Darhuber <sup>\*a</sup>

We have studied the motion of liquid droplets located in the contact zone of two soft solids that are pressed together inside a liquid. The driving force of the motion is the gradient of elastic contact pressure. Upon reaching the perimeter of the contact spot, the droplets coalesce with the surrounding bulk liquid either in a continuous or discontinuous fashion. Droplets that exhibit complete coalescence move with a speed proportional to the pressure gradient along their trajectory. However, droplets that undergo partial coalescence cascades (up to 9 were observed) do not. The latter also move significantly slower. We have identified surface roughness as a potential mechanism causing the contrasting behavior.

Received 4th October 2019,  
Accepted 16th January 2020

DOI: 10.1039/c9sm01992h

[rsc.li/soft-matter-journal](http://rsc.li/soft-matter-journal)

## 1 Introduction

The behavior of liquid confined between solids, of which at least one is soft and elastomeric, is important in a number of technological applications such as aquaplaning,<sup>1–11</sup> tribology, printing<sup>12–14</sup> and adhesion.<sup>15–20</sup> The stability of liquid films is highly desirable in tribological applications such as contact lenses and cartilage joints, where direct solid on solid contact would induce wear and frictional heating. However, the presence of low viscosity liquids such as water is generally a nuisance in the context of the adhesive joining of two surfaces, as liquids are essentially incompressible and thus prevent close contact and moreover reduce the effective Hamaker constant by up to a factor of 10.<sup>21</sup> For achieving maximum adhesion in wet environments the complete removal of liquid between the contacting materials is beneficial. However, in solid–liquid–solid dewetting complete removal of liquid is rare, *i.e.* temporarily trapped droplets are very frequently observed in the contact spot.<sup>22</sup> The focus of this manuscript is on the mechanism and dynamics of the expulsion of these droplets.

Brochard and coworkers have investigated the stability of uniform thin liquid films between soft solids and derived a scaling law for the growth dynamics of a circular dry spot.<sup>23–25</sup> They also presented a theory of spinodal dewetting of ultra thin films at soft interfaces.<sup>26</sup> Sneddon showed that the shape of an

inclusion characterized by a constant pressure in an incompressible elastic medium is an ellipse, except very near the perimeter of the inclusion.<sup>27</sup> Based on his work, Martin *et al.* showed that the shape of stationary droplets confined between soft elastic solids is (semi-)ellipsoidal and that the droplet footprint radius  $a_d$  scales as the square of the center height  $h_d$  of the droplet.<sup>22</sup>

This manuscript deals with the motion of droplets confined between a flat elastomer layer and an elastic hemisphere that is pressed into the layer. The non-uniform contact pressure gives rise to a pressure gradient in the contact zone, that drives the droplets radially outward. Our key finding is that at the perimeter of the contact area they merge with the outer liquid either completely in a single coalescence event or in a cascade of sequential partial coalescence events. We give an overview of various systems for which full and partial coalescence effects have been observed in the past in Section 6 and discuss their relevance to our findings. To gain insight into this experimental observation, we performed fully-coupled three-dimensional numerical simulations, which reproduce the droplet shape evolution very well. Moreover, we developed an analytical model that reproduces the scaling of the contact time of the droplet with the outer liquid upon coalescence well.

## 2 Experimental setup

Fig. 1(a) shows a sketch of the experimental geometry. An elastomer half-sphere is pressed onto a flat layer of the same material with liquid confined in between. The elastomer used was a silicone-based, heat-curable, two-component polymer

<sup>a</sup> Department of Applied Physics, Eindhoven University of Technology, The Netherlands. E-mail: a.a.darhuber@tue.nl

<sup>b</sup> Faculty of Science and Technology, University of Twente, The Netherlands

† Electronic supplementary information (ESI) available: Atomic force microscope measurements of the surface of a typical substrate (pdf). See DOI: 10.1039/c9sm01992h



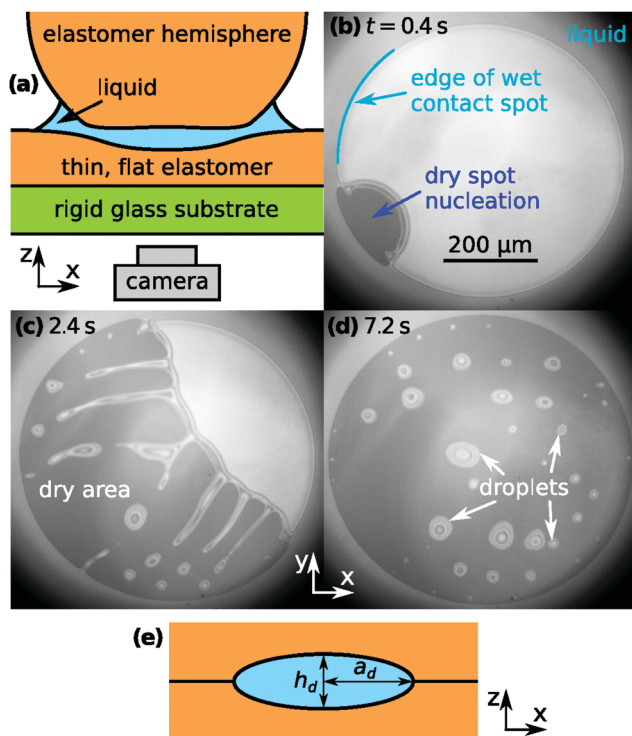


**Fig. 1** (a) Side-view sketch of the experimental geometry. (b–d) Microscope images of dry spot nucleation and dewetting in the wet contact zone between an elastic half-sphere and a flat elastic layer. Frequently droplets are created due to an instability of the dewetting rim. (e) Cross-sectional side-view sketch through a droplet with the maximum thickness  $h_d$  and footprint radius  $a_d$  indicated.

resin (Smooth-On, Encapso K, Young's modulus  $Y = 1.365$  MPa). The liquid is a perfluoropolyether (Solvay, Fomblin Y LVAC 14/6, average molecular weight 2500, viscosity  $\mu = 0.2646$  Pa s). The flat elastomer layer is attached to a glass substrate. The dynamics of the liquid is viewed from beneath the substrate with an inverted microscope. Details of the setup, the experimental procedures as well as the liquid and solid material properties are provided in ref. 28.

Fig. 1(b) shows a snapshot of the contact spot shortly after a dry spot nucleation event took place. Light reflected from the silicone–liquid and liquid–hemisphere interfaces gives rise to interference fringes [Fig. 1(b)–(d)], which allow to determine the film thickness distribution  $h(x,y)$  of the liquid. When dewetting starts, the liquid film thickness is essentially uniform throughout the contact spot. At this instant the liquid film thickness near the center of the contact spot was  $104 \pm 2$  nm and decreasing at a rate of  $2.4 \text{ nm s}^{-1}$  as<sup>24</sup>  $h$  evolves in time according to  $t^{-1/2}$ . Fig. 1(c) visualizes the growth process of the dry spot, which is accompanied by a pronounced instability of the dewetting rim. This leads to the formation of liquid threads that subsequently break up into droplets. Due to the radially increasing pressure gradient in the contact spot, droplets move radially outwards, the faster the closer they are to the edge of the contact spot.

According to ref. 29, silicone polymers may still contain uncrosslinked chains after curing, which can be extracted by

immersing the elastomer in a good solvent and subsequently deswelling it. We swelled different samples in toluene, *p*-xylene, ethyl acetate and 2-propanol for several days, refreshing the solution daily, then used a 1:1 mix by volume of the good solvent and ethanol for one day and pure ethanol for another day to deswell the samples. After this procedure we noted a mass loss of  $(22.5 \pm 0.1)\%$  in all cases. However, all solvents except 2-propanol induced partial disintegration or debonding of the elastomer layer. Consequently, we only used 2-propanol as the good solvent. The mass loss observed for our material system is considerably larger than that reported for Sylgard 184 in ref. 29. Nevertheless our layers remained optically clear and the surface remained smooth and flat.

## 3 Analytical model

### 3.1 Movement of droplets at soft interfaces

We consider a case where droplets occur after dewetting and aim to derive a simple description of their motion induced by the pressure gradient inside the contact spot. We define the elastocapillary length as  $L_{ec} = |S|/Y$ , where  $S \equiv \gamma_{ee} - 2\gamma_{el}$  is the spreading parameter. Here,  $\gamma_{ee}$  is the energy density of two identical elastomer surfaces in contact, and  $\gamma_{el}$  the elastomer–liquid surface energy density. Martin *et al.* considered the conformation of a droplet confined by soft, elastic interfaces.<sup>22</sup> When  $L_{ec}$  is much smaller than the droplet footprint radius  $a_d$ , then a droplet squeezed between a rigid plane and a soft solid in a region of uniform pressure will have the shape of a flat half-ellipsoid, with height<sup>22</sup>

$$h_d = \sqrt{\frac{6}{\pi} L_{ec} a_d} \text{ (half-ellipsoid)}. \quad (1)$$

When considering a droplet between two soft solids, the derivation is analogous to that in ref. 22, resulting in an additional prefactor of  $\sqrt{2}$

$$h_d = 2\sqrt{\frac{3}{\pi} L_{ec} a_d} \text{ (full ellipsoid)}. \quad (2)$$

We used eqn (2) to estimate the value of  $S$  from the observed droplet geometry. From our experiments we found  $S = (-8 \pm 2) \text{ mN m}^{-1}$ , corresponding to  $L_{ec} = (6 \pm 2) \text{ nm}$ . If the interfacial pressure distribution is not uniform, the droplet will move towards regions of lower pressure to minimize the elastic deformation energy. The speed of its motion will be determined by the balance of the viscous dissipation rate in the liquid and the elastic energy gain rate. Assuming that the droplet maintains a constant ellipsoidal shape, that the deformations are small and that the liquid flow inside the droplet can be determined from the Reynolds equation, an estimate of the droplet speed can be calculated.

The  $z$ -positions of the liquid–solid interfaces of the droplet in cylindrical coordinates (with origin at the droplet midpoint) are conforming to the ellipsoid shape

$$z_d(r) = \pm \frac{h_d}{2} \sqrt{1 - \frac{r^2}{a_d^2}}, \quad (3)$$



where  $h_d$  is the thickness of the droplet. The surface energy density  $u_A$  (work per unit area performed by pressure displacing the elastic surface by  $\delta$ ) is

$$u_A = \frac{1}{2}P\delta, \quad (4)$$

where  $P$  is the local pressure. The energy  $U_d$  needed to introduce a droplet at an interface between two elastomers is

$$U_d = 2 \int_0^{a_d} \frac{1}{2} P z_d(r) 2\pi r dr = \frac{\pi}{3} a_d^2 h_d P. \quad (5)$$

If the droplet is moving radially with a velocity  $v_d$  in a contact spot with pressure distribution  $P(r)$ , the energy gain rate is

$$\frac{\partial U_d}{\partial t} = \frac{\partial U_d}{\partial r} \frac{\partial r}{\partial t} = \frac{\partial U_d}{\partial r} v_d = \frac{\pi}{3} a_d^2 h_d v_d \frac{\partial P}{\partial r}. \quad (6)$$

Equating this expression with the total energy dissipation rate allows us to derive the droplet velocity. Following ref. 24 the viscous dissipation rate  $\dot{U}_\mu$  is approximately  $\mu(v_d/h_d)^2$  per unit volume. Thus the energy dissipation rate is approximately

$$\dot{U}_\mu \sim \mu \left( \frac{v_d}{h_d} \right)^2 \frac{2}{3} \pi a_d^2 h_d = \frac{2}{3} \pi \mu \frac{v_d^2}{h_d} a_d^2. \quad (7)$$

Equating eqn (7) and (6) yields an estimate for the radial droplet velocity

$$v_d(r) \sim \frac{2h_d^2}{\mu} \frac{\partial P}{\partial r} = \frac{24|S|a_d}{\pi\mu Y} \frac{\partial P}{\partial r}, \quad (8)$$

which is proportional to the contact pressure gradient.

### 3.2 Coalescence with outer bulk liquid

Droplets move towards the edge of the contact spot with the velocity  $v_d(r)$  given by eqn (8). Assuming that after the commencement of coalescence with the outer bulk liquid, the back of the droplet keeps moving with a constant velocity, the coalescence time  $\Delta t$  can be estimated as

$$\Delta t \approx \frac{2a_d}{v_d} \sim \frac{\pi\mu Y}{12|S|} \left( \frac{\partial P}{\partial r} \right)^{-1} \Bigg|_{r=r_{cs}-a_d}. \quad (9)$$

Assuming a Hertzian pressure distribution inside the contact spot<sup>30</sup>

$$P_H(r) = P_0 \sqrt{1 - \frac{r^2}{r_{cs}^2}}, \quad (10)$$

with  $P_0 \equiv 2r_{cs}Y/\pi R_L$  being the maximum pressure at the center, eqn (9) becomes

$$\Delta t_H \sim \frac{\pi^2 R_L \mu}{24|S|} \frac{\sqrt{(2 - \beta_d)\beta_d}}{1 - \beta_d}, \quad (11)$$

where we introduced the parameter  $\beta_d \equiv a_d/r_{cs}$ . For small  $\beta_d$  eqn (11) is approximately equal

$$\Delta t_H \sim \frac{\pi^2 R_L \mu}{24|S|} \sqrt{2} \frac{a_d}{r_{cs}}. \quad (12)$$

The JKR model<sup>31</sup> more accurately represents our system, as it additionally considers the surface energy of adhesion. For a JKR pressure distribution

$$P_{JKR}(r) = P_H(r) + P_1 \left( 1 - \frac{r^2}{r_{cs}^2} \right)^{-1/2}, \quad (13)$$

where  $P_1 \equiv -\sqrt{4|S|Y/\pi r_{cs}}$ , we find

$$\Delta t_{JKR} \sim \Delta t_H \left( 1 + \frac{R_L}{r_{cs}} \frac{\sqrt{\pi|S|}}{(2 - \beta_d)\beta_d} \right)^{-1}. \quad (14)$$

In the limit of  $\beta_d \rightarrow 0$  eqn (14) reduces to

$$\Delta t_{JKR} \sim \frac{\mu}{6} \sqrt{\frac{Y}{|S|}} \left( \frac{\pi a_d}{|S|} \right)^{3/2}. \quad (15)$$

We note that both the Hertzian and the JKR pressure profiles have an unphysical singularity of  $\partial P/\partial r$  at the edge of the contact spot. Both models do not represent accurately the pressure distribution around a contact line at a lengthscale equal to the elastocapillary length  $L_{ec}$ , which is approximately 10 nm for our material system. Since the droplet diameters we consider are typically a factor of thousand larger, the pressure profiles are expected to provide a suitable approximation.

## 4 Experimental results

### 4.1 Droplet motion

Fig. 2(a) shows microscope images of a droplet moving towards the edge of the contact spot. The red crosses denote the center of the contact spot. The white dotted line denotes the edge of the contact spot. The yellow dashed line is the centerline trajectory of the droplet in the radially outward direction. In Fig. 2(b), the time evolution of the radial intensity profiles  $I_c(d, t)$  through the center of the escaping droplet [dashed line in (a)] is visualized. The ordinate  $d \equiv r_{cs} - r$  quantifies the radial distance to the edge of the contact spot. The blue dotted line in Fig. 2(b) indicates the position of the midpoint of the droplet  $d_d(t)$  in time. Its slope  $|\dot{d}_d(t)|$  is equal to  $v_d$ .

Fig. 3 shows the correlation between the droplet velocity  $v_d$  and the local pressure gradient. The droplet speed  $v_d$  was determined by tracking the radial position of the center of the droplet – defined as halfway between the front and back of the droplet – in time. The pressure gradient is determined from the theoretical JKR pressure profile evaluated at the droplet center location. Right after their formation droplets usually have an irregular shape. The first datapoint for each curve in Fig. 3 corresponds to the moment when the droplet footprint has relaxed to a round shape. The last datapoints correspond to the frames right before coalescence with the outer bulk liquid.

The velocity profile of non-cascading droplets is generally linearly proportional to the local pressure gradient before coalescence, consistent with the behavior expected on hydrodynamic grounds. Two droplets that were observed to cascade only once also moved with a velocity proportional to  $|\partial P/\partial r|$



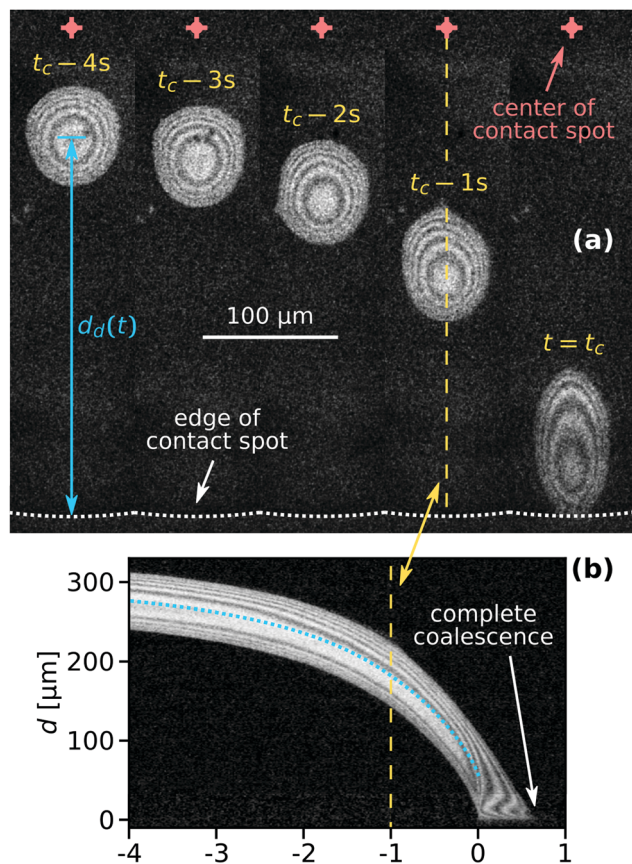


Fig. 2 (a) Microscope images of a droplet moving towards the edge of the contact spot. (b) Time evolution of the radial intensity profile  $I_c(d, t)$  through the center of the droplet visible in (a) which coalesces completely. The dashed lines both indicate  $I_c(d, t - t_c = 1 \text{ s})$ .

throughout most of their lifetime. In contrast, all droplets which cascaded at least twice exhibited a qualitatively different behavior. These droplets initially moved one to two orders of magnitude slower than the velocity predicted by the hydrodynamic model. Some even show a non-monotonic behavior, *i.e.* an initial slow-down and subsequent acceleration.

We fitted the velocity *vs.* pressure gradient curves in Fig. 3 with linear fit functions. In Fig. 4 we present the slopes  $\psi$  of these fit functions for the single- and non-cascading droplets as a function of droplet size  $a_d$  (crosses). According to eqn (8), the slope  $\psi = 24|S|a_d/(\pi\eta Y)$  is proportional to  $a_d$ . The gray solid line in Fig. 4 is a linear fit, which represents the experimental data well.

## 4.2 Droplet coalescence

The time  $t = t_c$  in Fig. 2(a) corresponds to the moment of first contact between the droplet and the outer bulk liquid. The coalescence process of radially moving droplets with the bulk liquid outside of the contact spot can proceed in a continuous or discontinuous fashion. Fig. 5 contrasts the two observed behaviours of either complete, continuous or partial, discontinuous coalescence. In Fig. 5(a)–(i), a droplet makes contact and continuously remains in contact with the outer liquid until it is entirely absorbed. In Fig. 5(j)–(r), the liquid bridge connecting the droplet and outer

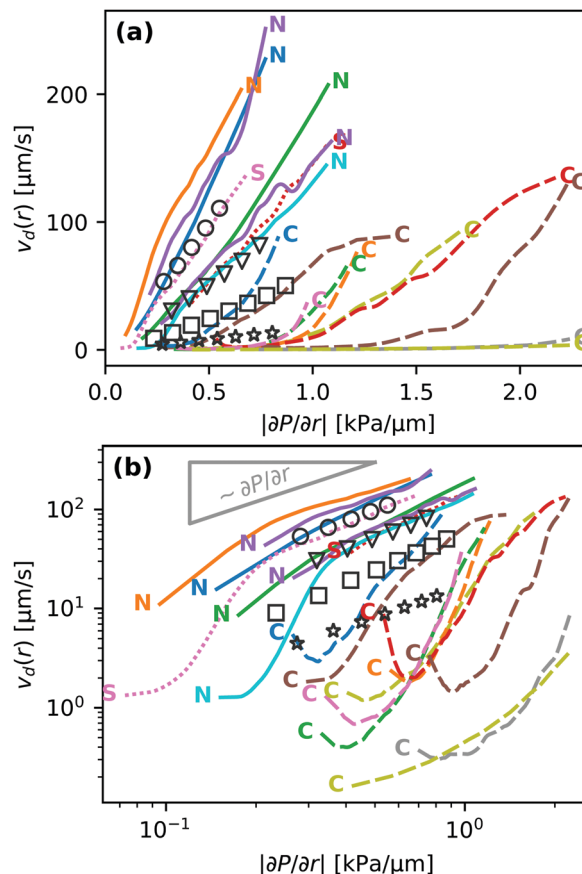


Fig. 3 Droplet velocity  $v_d$  plotted against the pressure gradient at the droplet center using (a) linear and (b) logarithmic axes. Non-cascading droplets (solid lines) are marked with 'N'. Droplets that cascaded once (dotted lines) or more than once (dashed lines) are labeled with 'S' or 'C', respectively. The open black symbols correspond to typical numerical results.

liquid displays a non-monotonic behaviour. It initially grows [Fig. 5(k) and (l)] then shrinks [Fig. 5(m)] and eventually disintegrates [Fig. 5(n)]. This cascading behaviour can occur multiple times during the lifetime of a droplet. Up to nine consecutive cascades were observed for a single droplet.

Fig. 6(a) shows a case where the droplet does not coalesce completely, but a much smaller droplet appears in proximity to the edge of the contact spot. Fig. 6(b) shows a plot of the radial centerline intensity profiles  $I_c(d, t)$  for a droplet cascading six times.

Fig. 6(c) compares the time history of the droplet footprint area of a non-cascading droplet and one that cascades five times. The latter shows a pronounced staircase-like morphology with a relatively uniform area reduction ratio  $\zeta_n \equiv A_n/A_{n-1}$ . Here,  $A_{n-1}$  and  $A_n$  denote the droplet footprint areas before and after its  $n$ -th cascade, respectively.

Fig. 7(a) shows systematic experimental data of the area reduction ratio  $\zeta_n$  of droplets undergoing their  $n$ -th cascade. After their first cascade most droplets become 2 to 6 times smaller. However, predominantly larger droplets (blue circles) sometimes produce secondary droplets that are more than 10 times smaller.



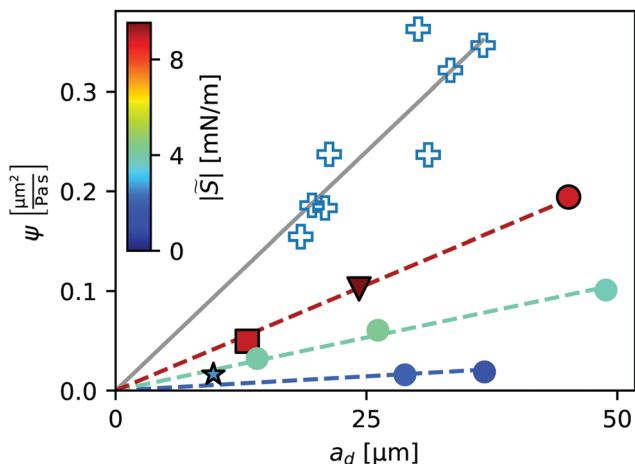


Fig. 4 Slope  $\psi$  of the velocity–pressure gradient curves shown in Fig. 3(a) for single- and non-cascading droplets. Open crosses represent experiments. Filled symbols represent numerical simulations, with their color indicating the value of the parameter  $|\tilde{S}|$ , to be discussed in Section 5. Filled symbols with black edges correspond to the numerical results in Fig. 3. Lines represent linear correlations  $\psi \sim a_d$ .

Fig. 7(b) shows the correlation between the area of a droplet  $A_{n-1}$  right before the  $n$ -th cascade and its contact time  $\Delta t_n$ , defined as the time from the start of coalescence to pinch-off, as indicated in Fig. 6(b). Larger droplets remain in contact with the outer bulk liquid for a longer time during a single cascade. The dashed and solid black lines and the dotted grey line represent eqn (11), (14) and (15), respectively. The black dots represent experiments using 2-propanol-treated samples, as described in ref. 29, to investigate the influence of uncrosslinked chains on the movement of droplets.

Fig. 8(a) shows the position of the rear  $d_r$ , the maximal half-width  $w_s$  and the neck half-width  $w_n$  of a droplet undergoing two partial coalescence cascades. The definitions of these parameters are illustrated in the inset. Fig. 8(b) shows the contact line speed at the back ( $v_r \equiv \dot{d}_r$ ), side ( $v_s \equiv \dot{w}_s$ ) and neck ( $v_n \equiv \dot{w}_n$ ) of the droplet, where a dot above a parameter indicates a time derivative. The two not visible positive maxima of  $v_n$  are at 110 and 60  $\mu\text{m s}^{-1}$ , respectively. We note that  $v_s$  reacts immediately to the formation of a liquid bridge ( $w_n > 0$ ) but  $v_r$  is delayed. This feature, as well as the positive values of  $v_s$  after breakup, is due to the droplet relaxing to a rounder shape after becoming elongated during the coalescence. To maintain a constant aspect ratio  $w_s/d_r$  the back would need to move twice as fast as the side.

## 5 Comparison with numerical simulations

In order to elucidate the qualitative difference between cascading and non-cascading droplets we turn to numerical simulations for gaining further insight. We used the same fully-coupled, three-dimensional numerical model that is described in detail in ref. 28. We combine the stationary Cauchy momentum equation for soft, linear elastic materials with the Reynolds equation for thin film

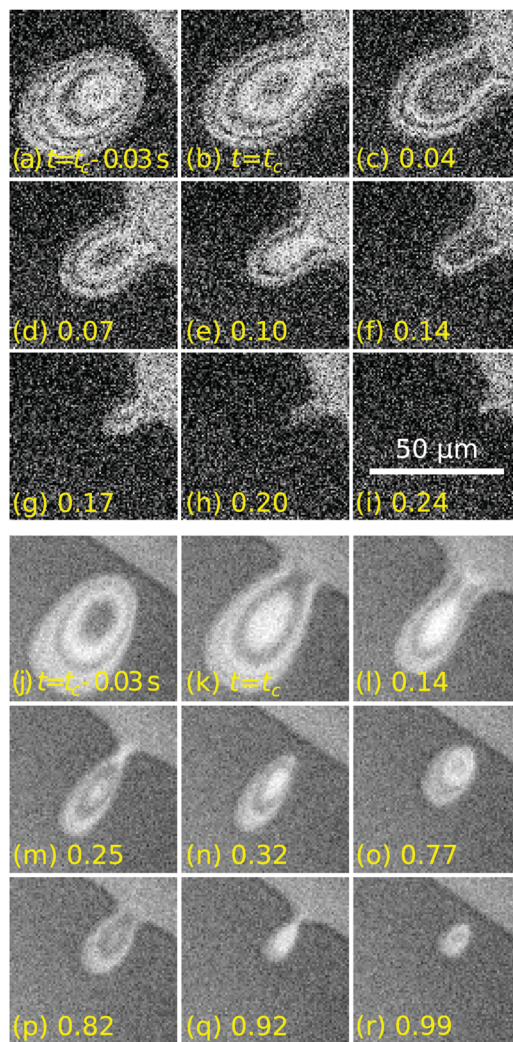


Fig. 5 The coalescence of moving droplets with the bulk liquid outside of the contact spot can proceed in a continuous (a–i) or discontinuous (j–r) fashion. The indicated time increments are given relative to the frames (b and k) where coalescence started. The scale bar in (i) applies to all images.

flow and apply a disjoining pressure formalism to implement the partial wettability. We solved the equations using finite element software COMSOL Multiphysics. In our numerical simulations we disregard the dewetting process visible in Fig. 1(b) but rather use an initial condition analogous to the first frame of Fig. 2(a). A single droplet of given volume is released at a certain distance from the center of the contact spot.

The circles in Fig. 4 represent numerical simulations, with their color indicating the value of the parameter

$$|\tilde{S}| \equiv \frac{\pi Y h_d^2}{6 a_d}, \quad (16)$$

obtained by extracting the footprint radius  $a_d$  and height  $h_d$  of a droplet. Eqn (16) is derived from eqn (1) for half-ellipsoidal droplets, but based on values of  $h_d$  and  $a_d$  taken from the simulations. The dashed lines are linear relations  $\psi \sim a_d$ , which match the numerical results reasonably well, again consistent with eqn (8).



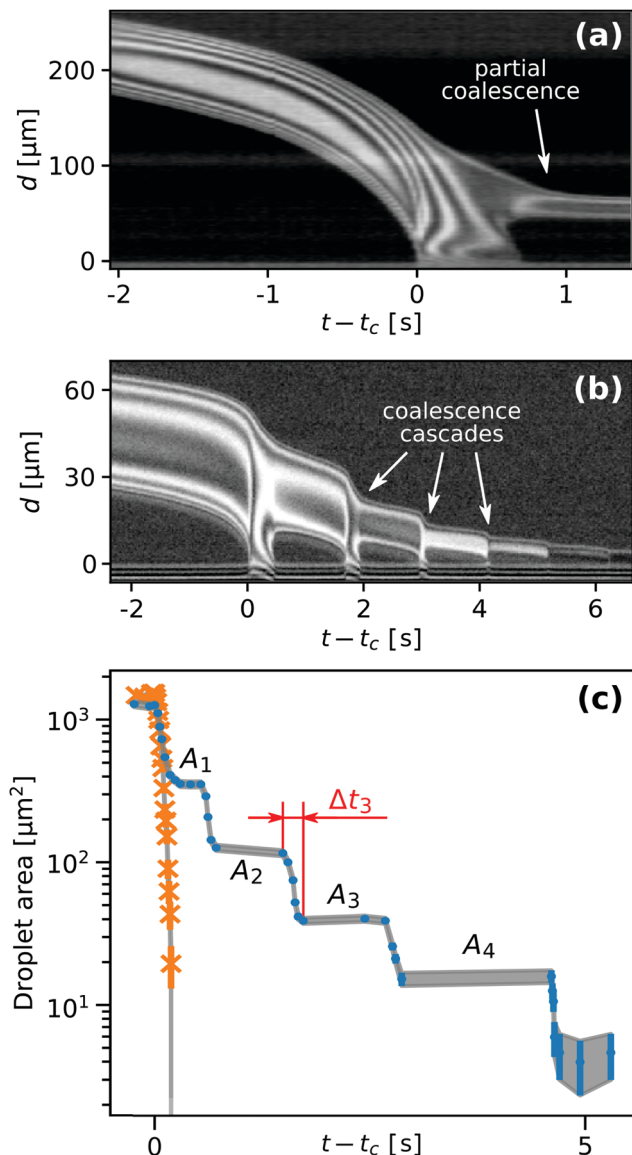


Fig. 6 Plot of the radial centerline intensity profiles  $I_c(d,t)$  for a droplet which (a) coalesces only partially and leaves a smaller droplet behind and (b) one that cascaded six times. (c) Droplet footprint area as a function of time. The orange crosses and blue circles correspond to the data shown in Fig. 5(a)–(i) and (j)–(r), respectively.

Fig. 9 compares experimental droplet morphologies with numerical simulations. The dotted white lines in Fig. 9(a)–(e) mark the edge of the contact spot. The solid lines in Fig. 9(f)–(j) are lines of equal liquid film thickness, similar to the interference fringes in (a)–(e). The overall shape of the simulated droplets agrees very well with the experimentally observed ones.

Fig. 10 shows snapshots from three different simulations of escaping droplets, where we have varied the droplet footprint radius  $a_d$  as well as the parameter  $|\tilde{S}|$ . In Fig. 10(i)–(l)  $a_d$  is twice as large as in (a)–(h), whereas  $|\tilde{S}|$  is twice as high in Fig. 10(e)–(l) compared to (a)–(d). In other words, rows (a)–(d) and (i)–(l) share the same  $L_{ec}/a_d$  ratio, whereas row (e)–(h) has twice as large a ratio. We note that the similar morphology evolution of

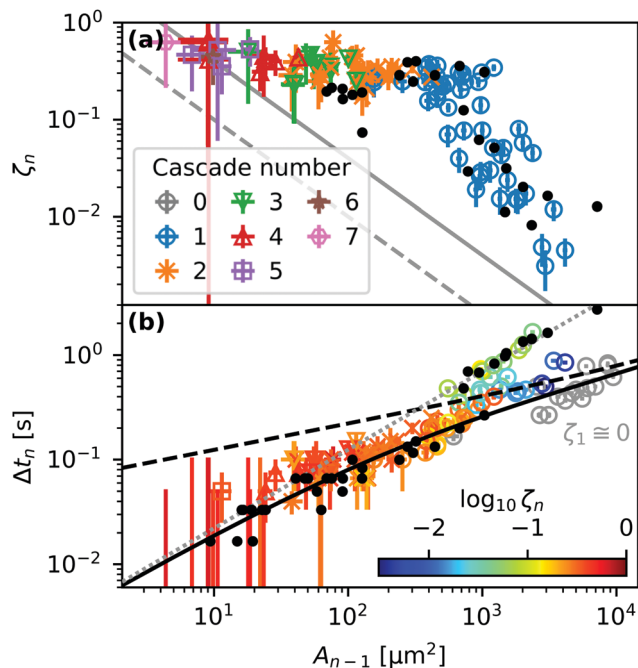


Fig. 7 (a) Area reduction ratio  $\zeta_n$  and (b and c) contact time  $\Delta t_n$  of droplets with footprint area  $A_{n-1}$  undergoing their  $n$ -th cascade. The solid and dashed lines in (a) represent the resolution limits of experimentally observable  $\zeta_n$  values for two used microscope magnifications. The color of the symbols in (b) represents the  $\zeta_n$  value as indicated by the colorbar. Gray circles in (b) correspond to fully coalescing, non-cascading droplets. The dashed and solid black lines and the dotted grey line represent eqn (11), (14) and (15), respectively. Black dots represent measurements on substrates treated with 2-propanol.

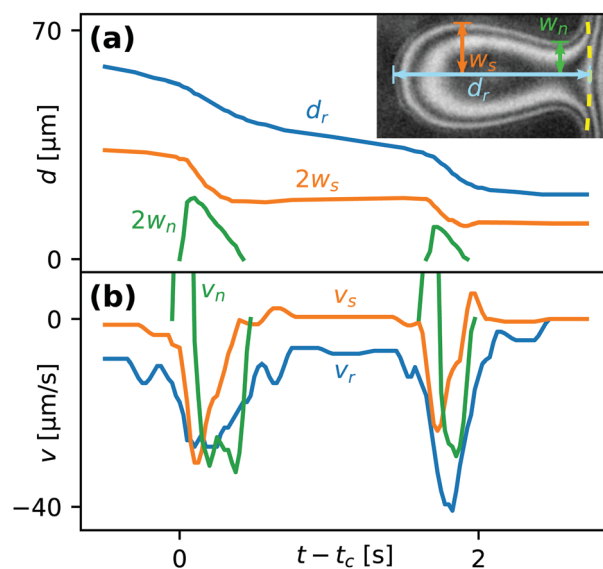


Fig. 8 (a) Time dependence of the rear position  $d_r$ , maximal width  $w_s$  and neck width  $w_n$  of a droplet undergoing two coalescence cascades. Inset: Definitions of  $d_r$ ,  $w_s$  and  $w_n$ . The contact spot edge is marked with a dashed yellow line. (b) Contact line speed at the rear ( $v_r$ ), side ( $v_s$ ) and neck ( $v_n$ ) of the droplet.

Fig. 10(a)–(d) and (i)–(l) may be related to these cases having the same ratio of the elastocapillary length  $L_{ec}$  to the footprint



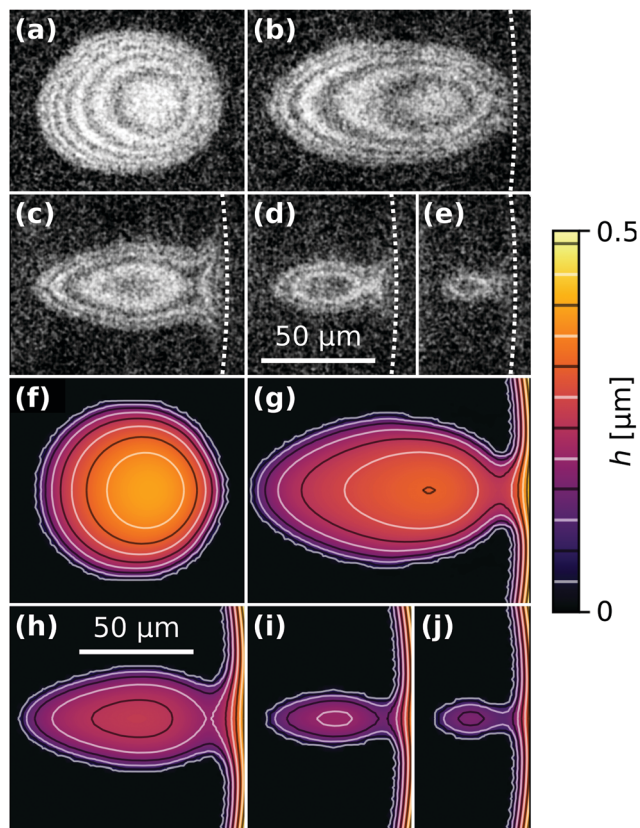


Fig. 9 Snapshots from an experiment (a)–(e) and a numerical simulation (f)–(j) showing similar droplet morphologies before and during complete coalescence with the outer bulk liquid, *i.e.* without cascading. The contours in (f)–(j) are lines of equal film thickness, similar to the interference fringes in (a)–(e). The (identical) scale bars in (d) and (h) apply to all images.

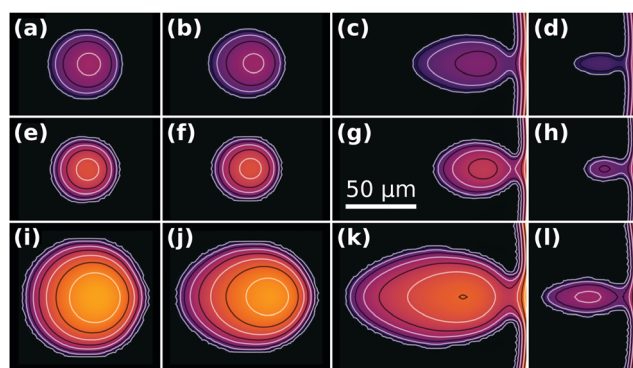


Fig. 10 Snapshots from three numerical simulations. Columns 1–4 show droplets when  $d/r_{cs} = 0.45, 0.3$ , at the start of coalescence and during coalescence, respectively. Row (a)–(d) shows a droplet with initial  $L_d = 52 \mu\text{m}$  and  $|\tilde{S}| = 4.2 \text{ mN m}^{-1}$ . The value of  $|\tilde{S}|$  was twice as high in row (e)–(h) as in row (a)–(d), *i.e.*  $|\tilde{S}| = 9.5 \text{ mN m}^{-1}$  and  $2a_d = 49 \mu\text{m}$ . The droplet was twice as wide in row (i)–(l) as in row (e)–(h), *i.e.*  $2a_d = 90 \mu\text{m}$  and  $|\tilde{S}| = 8.9 \text{ mN m}^{-1}$ .

radius  $a_d$ . Similarly, the higher ratio in Fig. 10(e)–(h) may be responsible for the less elongated shape throughout the droplet escape history.

## 6 Discussion

So-called partial coalescence and coalescence cascades have been observed for droplets contacting other droplets or flat liquid–liquid or liquid–air interfaces.<sup>32–44</sup> Usually partial coalescence of pure liquids requires a high Weber number *i.e.* sufficient inertia and the propagation of capillary waves, *i.e.* an Ohnesorge number below a critical value. In our case  $We \equiv \rho v_d^2 a_d / |\tilde{S}| \approx 10^{-8}$  and  $Oh \equiv \mu / \sqrt{\rho |\tilde{S}| a_d} \approx 10$ , therefore capillary waves are not present, as the system is strongly dominated by viscous forces. Glass *et al.* studied the effect of water-soluble polymers on coalescence cascades of organic liquid drops at an organic liquid–water interface.<sup>45</sup> Sartor and Abbott and Beard *et al.* considered the effect of dissimilar electrical droplet charges on the coalescence of colliding droplets and found that charge differences promote complete coalescence.<sup>46–48</sup> Ristenpart *et al.* studied the droplet rebound from a liquid–liquid interface subject to an applied perpendicular electric field.<sup>49</sup> Beard *et al.* showed that a reduction in air pressure promoted contact, thereby reducing the likelihood of bouncing and increasing that of permanent coalescence.<sup>50</sup> Feng *et al.* investigated the effect of non-Newtonian rheology on the coalescence dynamics.<sup>51,52</sup> When either the drop or the surrounding phase is a polymer solution, viscoelasticity tends to delay the break-up of secondary drops and can suppress partial coalescence altogether, as large tensile polymer stresses resist the stretching and thinning of the fluid neck. Kuznicki *et al.* considered the effect of electrolyte concentration on coalescence cascades of oil droplets.<sup>53</sup> De Malmazet *et al.* showed that the presence of micro-particles reduces drop lifetimes and promotes complete coalescence.<sup>54</sup> Blanchette *et al.* studied the influence of soluto-capillary Marangoni stresses on drop coalescence.<sup>55</sup> Surfactants can enhance or weaken partial coalescence effects, depending on the concentrations and the induced surface elasticity.<sup>56–61</sup>

For our system, inertia is negligible and there are no propagating capillary or elastic waves induced by the droplet motion. Although the dependence of contact time on droplet radius  $\Delta t \sim R^{3/2}$  as observed by *e.g.* Thoroddsen and Takehara<sup>33</sup> agrees with the scaling  $\Delta t \sim a_d^{3/2}$  in eqn (15) this agreement is coincidental, as the prefactors depend on unrelated material properties. Our material system is not susceptible to surfactant adsorption. Moreover, we have measured electric surface charge distribution induced by solid-on-solid contact and separation, but it was below the detection limit ( $10^{12}$  ions per  $\text{m}^2$ ).<sup>62,63</sup> Since the droplets move smoothly and continuously without stick-slip behavior and since they maintain a round and mirror-symmetric morphology, it is highly unlikely that surface irregularities and defects are responsible for the slow motion and the cascading behavior. Non-homogeneities tend to cause irregular droplet footprints and non-monotonic velocity profiles.

We speculate that the coalescence cascades are merely a consequence of the slow contact line speed. The latter implies that the aspect ratio of the liquid bridge becomes slender such that it is susceptible to break-up. This is analogous to the partial coalescence mechanism for liquid droplets suggested by Blanchette and Bigioni: if capillary waves can sufficiently delay the vertical (in our case: radial) collapse, pinch off will occur



and a smaller drop will be left above the interface (in our case: near the edge of the contact spot).<sup>37,39</sup> Instead of capillary oscillations delaying the forward motion of the rear end of the free droplets studied by Blanchette and Bigioni, the delay in our case is likely of a different nature. This may hint at the presence of a dissipation mechanism that depends non-linearly on the droplet velocity. Such a dissipation mechanism could explain the observed variation of the droplet speeds by two orders of magnitude in Fig. 3.

In our numerical simulations we consider a homogeneous surface and bulk composition so far. The simulated droplets move according to hydrodynamical expectations and exhibit complete coalescence without cascading behavior. We have attempted to reproduce the slow yet smooth droplet motion seen in the experiments in Fig. 3 by modulating geometric and material properties of our system. Specifically, we considered the influence of surface roughness as well as spatial modulations of the spreading parameter  $|S|$  and Young's modulus  $Y$ . As for the latter two, we generally found that for experimentally conceivable parameter variations, the reduction in contact line speed was far less than two orders of magnitude. In the following subsection we report on the effect of surface roughness.

### 6.1 Influence of surface roughness

In order to study the effects of surface roughness we considered a two dimensional axisymmetric system for computational efficiency. We introduced a sinusoidal surface profile of the rigid substrate with wavelength  $\lambda$  and amplitude  $A$ . In order to nucleate a dry spot and obtain a receding contact line, we introduce a topological defect centered around  $r = 0$  shown by the gray shaded area in Fig. 11(a). Dotted and dash-dotted lines indicate the sinusoidal surface profiles for two different sets of values of  $\lambda$  and  $A$ . In order to speed up calculations, the pattern starts at a certain radial position  $r_0$  and extends only over a few wavelengths. The solid and dashed lines correspond to the  $z$ -position of the elastomer-liquid interface. The inset shows the entire contact spot from its center to its edge.

Fig. 11(b) shows the time evolution of the non-dimensional elastomer-liquid interface profile. The contact line recedes to the right. For clarity, we non-dimensionalized the  $r$  and  $z$  coordinates using the scales of  $\lambda$  and  $A$  in order to collapse the two surface profiles. The two families of curves represent constant time increments of either 1 or 10 milliseconds, corresponding to two different sets of  $\lambda$  and  $A$ . In the case of the smaller amplitude ( $A = 20$  nm, dashed orange lines) the contact line moves continuously, though at a non-constant speed  $v_{cl}$ .  $v_{cl}$  is considerably faster when moving up a slope compared to moving down. In the case of the larger amplitude ( $A = 50$  nm, solid blue lines), the contact line gets pinned on the descending slope, despite the  $A/\lambda$  aspect ratio being the same as in the first case. The contact line advances by nucleating a secondary dry spot at the adjacent apex of the surface roughness profile. At the same time liquid becomes entrapped in the "valleys", as indicated by the dashed arrow.

In Fig. 12 is plotted the contact line speed  $v_{avg} \equiv \langle v_{cl} \rangle$  averaged over two wavelengths of the roughness profile. Filled symbols signify liquid entrapment. The average contact line

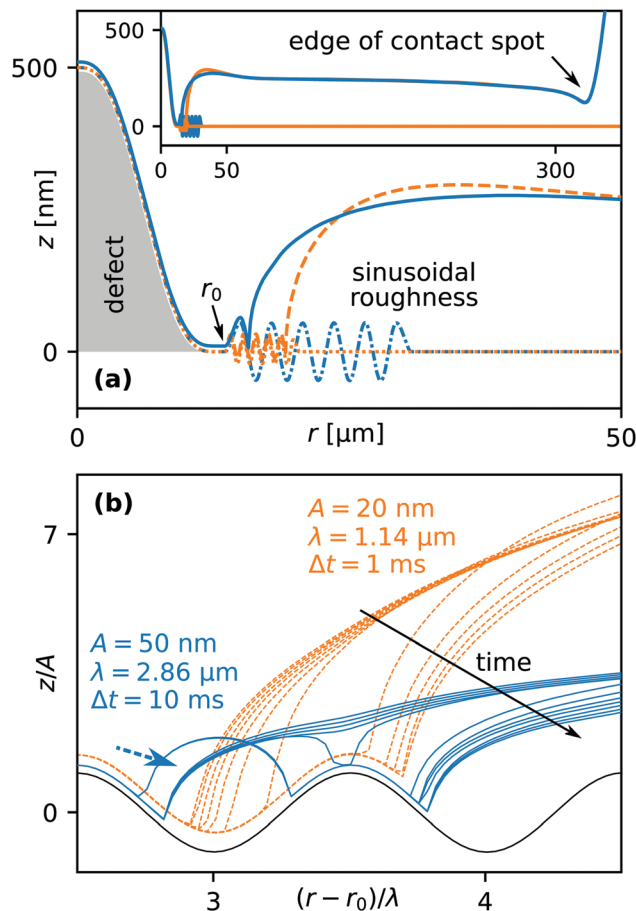


Fig. 11 Simulated liquid film thickness profiles for non-flat substrate topologies. (a) The dash-dotted blue line shows the substrate topology, with a sinusoidal pattern of amplitude  $A = 50$  nm and wavelength  $\lambda = 2.86$   $\mu\text{m}$ . The solid blue line represents the  $z$ -position of the elastomer-liquid interface. The dashed and dotted orange lines represent a similar simulation with  $A = 20$  nm and the same  $A/\lambda$  ratio. (b) Time evolution of the non-dimensional elastomer-liquid interface profile. The two families of curves represent constant time increments of either 1 or 10 ms.

speed strongly decreases with increasing amplitude  $A$ , more rapidly for smaller values of the wavelength  $\lambda$ , *i.e.* higher aspect ratios  $A/\lambda$ . Due to computational limitations concerning the minimum mesh size, we could not explore sub-micron values of  $\lambda$ . However, it is clear from Fig. 12 that especially for small  $\lambda$  a significant reduction in the average velocity is observed, at least by one order of magnitude. Extrapolating towards sub-micron wavelengths, these results indicate that even with a roughness amplitude so small that it would not be noticeable using optical interferometry, the contact line speed could be reduced by a similar order of magnitude as observed in the experiments in Fig. 3. Due to the limited spatial resolution of our optical setup, the corresponding spatial modulation of the contact line speed  $v_{cl}$  could not be resolved and would appear as smooth. Based on these results we hypothesize that the non-hydrodynamic motion of the droplets could be caused by surface roughness.

### 6.2 Influence of uncrosslinked chains

Despite the 22.5% mass loss after 2-propanol treatment, the observed droplet dynamics remained the same. The data points



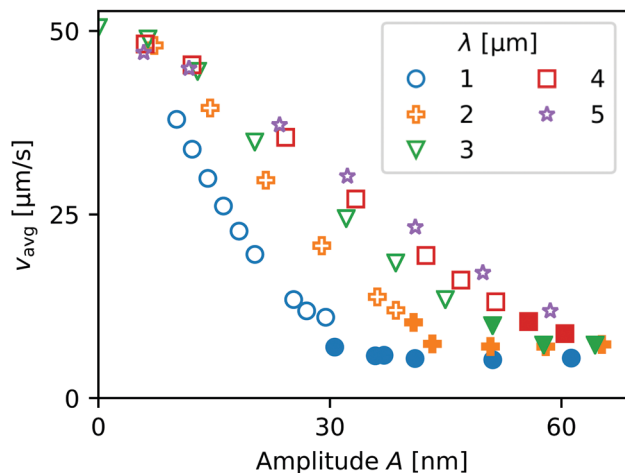


Fig. 12 Average speed of the receding contact line moving across the pattern in Fig. 11(a), as a function of the pattern wavelength  $\lambda$  and amplitude  $A$ . Larger amplitudes and smaller wavelengths can slow down the movement by an order of magnitude. Filled points signify liquid entrapment.

in Fig. 7 overlap with the ones obtained with not-treated samples. We conclude that uncrosslinked chains do not influence the droplet motion in our case. In contrast, in ref. 29 the uncrosslinked chains had a drastic effect on sessile droplet motion. We believe that this qualitative difference might be related to the much higher interfacial tension of the liquids (glycerol-water mixtures) used by these authors as well as the presence of a deformable liquid-air interface, which is absent in our case.

## 7 Conclusion

We have studied the escape dynamics of liquid droplets from the contact zone of an elastic hemisphere pressed into a soft solid layer. The driving force of the motion is the radial pressure gradient. Upon reaching the edge of the contact spot, droplets merge with the outer bulk liquid either in a continuous or discontinuous fashion. In the first case a single ‘complete’ coalescence event is observed, whereas in the latter case a cascade of partial coalescence events occurs. Numerical simulations could reproduce the shape and escape dynamics of the non-cascading droplets qualitatively well. The coalescence time of these droplets are well described by a simple analytical model.

Droplets that undergo a coalescence cascade tend to move much slower than droplets that merge in a single coalescence event. Moreover, the speed of motion of the cascading droplets is not proportional to the local pressure gradient. Using numerical simulations, we have investigated surface roughness and spatial modulations of Young’s modulus and the spreading parameter as potential mechanisms that could slow the droplets down. As for the latter two, we generally found that for experimentally conceivable parameter variations, the reduction in contact line speed was far less than two orders of magnitude. In contrast, surface roughness induced a speed reduction comparable with the experimental observations and is thus a viable candidate for the responsible mechanism. Solvent extraction of

uncrosslinked chains in the elastomer did not have an impact on the observed droplet dynamics.

## Conflicts of interest

There are no conflicts of interest to declare.

## Acknowledgements

We would like to thank Boija He for his help with surface charge measurements. We would like to thank an anonymous referee for pointing our attention towards ref. 29 and the significance of uncrosslinked polymer chains on the dynamics of adhering droplets. This project has received funding from the European Union’s Horizon 2020 research and innovation programme under the Marie Skłodowska-Curie grant agreement No. 642861.

## References

- 1 H. Grogger and M. Weiss, Calculation of the hydroplaning of a deformable smooth-shaped and longitudinally-grooved tire, *Tire Sci. Technol.*, 1997, **25**(4), 265–287.
- 2 B. N. J. Persson, U. Tartaglino, O. Albohr and E. Tosatti, Sealing is at the origin of rubber slipping on wet roads, *Nat. Mater.*, 2004, **3**(12), 882.
- 3 B. N. J. Persson, U. Tartaglino, O. Albohr and E. Tosatti, Rubber friction on wet and dry road surfaces: the sealing effect, *Phys. Rev. B*, 2005, **71**(3), 035428.
- 4 J. R. Cho, H. W. Lee, J. S. Sohn, G. J. Kim and J. S. Woo, Numerical investigation of hydroplaning characteristics of three-dimensional patterned tire, *Eur. J. Mech. A-Soild*, 2006, **25**(6), 914–926.
- 5 M. Varenberg and S. N. Gorb, Hexagonal surface micropattern for dry and wet friction, *Adv. Mater.*, 2009, **21**(4), 483–486.
- 6 T. F. Fwa, S. S. Kumar, K. Anupam and G. P. Ong, Effectiveness of tire-tread patterns in reducing the risk of hydroplaning, *Transp. Res. Rec.*, 2009, **2094**(1), 91–102.
- 7 S. Vincent, A. Sarthou, J. P. Caltagirone, F. Sonilhac, P. Février and C. Mignot, *et al.*, Augmented Lagrangian and penalty methods for the simulation of two-phase flows interacting with moving solids. Application to hydroplaning flows interacting with real tire tread patterns, *J. Comput. Phys.*, 2011, **230**(4), 956–983.
- 8 B. Zheng, X. Huang, W. Zhang, R. Zhao and S. Zhu, Adhesion Characteristics of Tire-Asphalt Pavement Interface Based on a Proposed Tire Hydroplaning Model, *Adv. Mater. Sci. Eng.*, 2018, 5916180.
- 9 H. F. Bohn and W. Federle, Insect aquaplaning: nepenthes pitcher plants capture prey with the peristome, a fully wettable water-lubricated anisotropic surface, *Proc. Natl. Acad. Sci. U. S. A.*, 2004, **101**(39), 14138–14143.
- 10 T. Nishi, Influence of lubricant properties and contacting velocity on real contact formation between rubber and glass in a contact process, *Tribol. Int.*, 2018, **127**, 240–244.



- 11 T. Nishi, Influence of curvature radius, elastic modulus, and contact velocity on real contact formation between rubber hemisphere and glass plate during contact process under a water-lubricated condition, *Tribol. Int.*, 2019, **130**, 284–288.
- 12 A. A. Darhuber, S. M. Troian and S. Wagner, Physical mechanisms governing pattern fidelity in microscale offset printing, *J. Appl. Phys.*, 2001, **90**(7), 3602–3609.
- 13 D. Kang, E. Lee, H. Kim, Y. M. Choi, S. Lee and I. Kim, *et al.*, Investigation on synchronization of the offset printing process for fine patterning and precision overlay, *J. Appl. Phys.*, 2014, **115**(23), 234908.
- 14 H. M. Sauer, D. Daume and E. Dörsam, Lubrication theory of ink hydrodynamics in the flexographic printing nip, *J. Print Media Technol. Res.*, 2015, **4**, 163–172.
- 15 C. Auner, U. Palfinger, H. Gold, J. Kraxner, A. Haase and T. Haber, *et al.*, Residue-free room temperature UV-nano-imprinting of submicron organic thin film transistors, *Org. Electron.*, 2009, **10**(8), 1466–1472.
- 16 C. Auner, U. Palfinger, H. Gold, J. Kraxner, A. Haase and T. Haber, *et al.*, High-performing submicron organic thin-film transistors fabricated by residue-free embossing, *Org. Electron.*, 2010, **11**(4), 552–557.
- 17 S. J. Choi, D. Tahk and H. Yoon, Spontaneous dewetting-induced residue-free patterning at room temperature, *J. Colloid Interface Sci.*, 2009, **340**(1), 74–81.
- 18 H. Yoon, S. H. Lee, S. H. Sung, K. Y. Suh and K. Char, Mold design rules for residual layer-free patterning in thermal imprint lithography, *Langmuir*, 2011, **27**(12), 7944–7948.
- 19 H. Yoon, H. Lee and W. B. Lee, Toward residual-layer-free nanoimprint lithography in large-area fabrication, *Korea-Aust. Rheol. J.*, 2014, **26**(1), 39–48.
- 20 M. Leitgeb, D. Nees, S. Ruttloff, U. Palfinger, J. Götz and R. Liska, *et al.*, Multilength scale patterning of functional layers by roll-to-roll ultraviolet-light-assisted nanoimprint lithography, *ACS Nano*, 2016, **10**(5), 4926–4941.
- 21 J. N. Israelachvili, *Intermolecular and surface forces*, Academic Press, 2011.
- 22 P. Martin, P. Silberzan and F. Brochard-Wyart, Sessile droplets at a solid/elastomer interface, *Langmuir*, 1997, **13**(18), 4910–4914.
- 23 F. Brochard-Wyart and P. G. de Gennes, Dewetting of a water film between a solid and a rubber, *J. Phys.: Condens. Matter*, 1994, **6**(23A), A9.
- 24 P. Martin and F. Brochard-Wyart, Dewetting at soft interfaces, *Phys. Rev. Lett.*, 1998, **80**(15), 3296.
- 25 A. Martin, A. Buguin and F. Brochard-Wyart, Dewetting nucleation centers at soft interfaces, *Langmuir*, 2001, **17**(21), 6553–6559.
- 26 A. Martin, O. M. Rossier, A. Buguin, P. Auroy and F. Brochard-Wyart, Spinodal dewetting of thin liquid films at soft interfaces, *Eur. Phys. J. E*, 2000, **3**(4), 337–341.
- 27 I. N. Sneddon, The distribution of stress in the neighbourhood of a crack in an elastic solid, *Proc. R. Soc. London, Ser. A*, 1946, **187**(1009), 229–260.
- 28 M. Chudak, J. S. Kwaks, J. H. Snoeijer and A. A. Darhuber, Non-axisymmetric elastohydrodynamic solid-liquid-solid dewetting: experiments and numerical modelling, *Eur. Phys. J. E*, 2020, **43**(1), 2.
- 29 A. Hourlier-Fargette, A. Antkowiak, A. Chateauminois and S. Neukirch, Role of uncrosslinked chains in droplets dynamics on silicone elastomers, *Soft Matter*, 2017, **13**(19), 3484–3491.
- 30 H. R. Hertz, Über die Berührung fester elastischer Körper, *J. Pure Appl. Math.*, 1882, **92**, 156–171.
- 31 K. L. Johnson, K. Kendall and A. D. Roberts, Surface energy and the contact of elastic solids, *Proc. R. Soc. London, Ser. A*, 1971, **324**(1558), 301–313.
- 32 G. E. Charles and S. G. Mason, The mechanism of partial coalescence of liquid drops at liquid/liquid interfaces, *J. Colloid Sci.*, 1960, **15**(2), 105–122.
- 33 S. T. Thoroddsen and K. Takehara, The coalescence cascade of a drop, *Phys. Fluids*, 2000, **12**(6), 1265–1267.
- 34 G. A. Bach, D. L. Koch and A. Gopinath, Coalescence and bouncing of small aerosol droplets, *J. Fluid Mech.*, 2004, **518**, 157–185.
- 35 E. M. Honey and H. P. Kavehpour, Astonishing life of a coalescing drop on a free surface, *Phys. Rev. E*, 2006, **73**(2), 027301.
- 36 X. Chen, S. Mandre and J. J. Feng, Partial coalescence between a drop and a liquid-liquid interface, *Phys. Fluids*, 2006, **18**(5), 051705.
- 37 F. Blanchette and T. P. Bigioni, Partial coalescence of drops at liquid interfaces, *Nat. Phys.*, 2006, **2**(4), 254.
- 38 T. Gilet, K. Mulleners, J. P. Lecomte, N. Vandewalle and S. Dorbolo, Critical parameters for the partial coalescence of a droplet, *Phys. Rev. E*, 2007, **75**(3), 036303.
- 39 F. Blanchette and T. P. Bigioni, Dynamics of drop coalescence at fluid interfaces, *J. Fluid Mech.*, 2009, **620**, 333–352.
- 40 F. H. Zhang, E. Q. Li and S. T. Thoroddsen, Satellite formation during coalescence of unequal size drops, *Phys. Rev. Lett.*, 2009, **102**(10), 104502.
- 41 B. Ray, G. Biswas and A. Sharma, Generation of secondary droplets in coalescence of a drop at a liquid-liquid interface, *J. Fluid Mech.*, 2010, **655**, 72–104.
- 42 I. S. Klyuzhin, F. Ienna, B. Roeder, A. Wexler and G. H. Pollack, Persisting water droplets on water surfaces, *J. Phys. Chem. B*, 2010, **114**(44), 14020–14027.
- 43 H. P. Kavehpour, Coalescence of drops, *Annu. Rev. Fluid Mech.*, 2015, **47**, 245–268.
- 44 A. Fakhari, D. Bolster and L. S. Luo, A weighted multiple-relaxation-time lattice Boltzmann method for multiphase flows and its application to partial coalescence cascades, *J. Comput. Phys.*, 2017, **341**, 22–43.
- 45 J. E. Glass, R. D. Lundberg and F. E. Bailey Jr, The effect of polymeric hydrocolloids on the partial coalescence of liquid drops at liquid-liquid interfaces, *J. Colloid Interface Sci.*, 1970, **33**(4), 491–507.
- 46 J. D. Sartor and C. E. Abbott, Some details of coalescence and charge transfer between freely falling drops in different electrical environments, *J. Rech. Atmos.*, 1972, **6**, 479–493.
- 47 H. T. Ochs III, K. V. Beard, R. R. Czyns, N. F. Laird, D. E. Schaufelberger and D. J. Holdridge, Collisions between small precipitation drops. Part I: laboratory measurements of bounce, coalescence, and temporary coalescence, *J. Atmos. Sci.*, 1995, **52**(12), 2258–2275.



- 48 K. V. Beard and H. T. Ochs III, Collisions between small precipitation drops. Part II: formulas for coalescence, temporary coalescence, and satellites, *J. Atmos. Sci.*, 1995, **52**(22), 3977–3996.
- 49 W. D. Ristenpart, J. C. Bird, A. Belmonte, F. Dollar and H. A. Stone, Non-coalescence of oppositely charged drops, *Nature*, 2009, **461**(7262), 377.
- 50 K. V. Beard, H. T. Ochs III and S. Liu, Collisions between small precipitation drops. Part III: laboratory measurements at reduced pressure, *J. Atmos. Sci.*, 2001, **58**(11), 1395–1408.
- 51 P. Yue, C. Zhou and J. J. Feng, A computational study of the coalescence between a drop and an interface in Newtonian and viscoelastic fluids, *Phys. Fluids*, 2006, **18**(10), 102102.
- 52 X. Chen, S. Mandre and J. J. Feng, An experimental study of the coalescence between a drop and an interface in Newtonian and polymeric liquids, *Phys. Fluids*, 2006, **18**(9), 092103.
- 53 N. P. Kuznicki, M. Krasowska, P. M. F. Sellaperumage, Z. Xu, J. Masliyeh and J. Ralston, *et al.*, Cascade partial coalescence phenomena at electrolyte-oil interfaces and determination of bounds for the surface potential, *Soft Matter*, 2013, **9**(17), 4516–4523.
- 54 E. de Malmazet, F. Risso, O. Masbernat and V. Pauchard, Coalescence of contaminated water drops at an oil/water interface: influence of micro-particles, *Colloids Surf., A*, 2015, **482**, 514–528.
- 55 F. Blanchette, L. Messio and J. W. M. Bush, The influence of surface tension gradients on drop coalescence, *Phys. Fluids*, 2009, **21**(7), 072107.
- 56 Y. Amarouchene, G. Cristobal and H. Kellay, Noncoalescing drops, *Phys. Rev. Lett.*, 2001, **87**(20), 206104.
- 57 D. Fell, M. Sokuler, A. Lembach, T. F. Eibach, C. Liu and E. Bonaccorso, *et al.*, Drop impact on surfactant films and solutions, *Colloid Polym. Sci.*, 2013, **291**(8), 1963–1976.
- 58 D. W. Martin and F. Blanchette, Simulations of surfactant effects on the dynamics of coalescing drops and bubbles, *Phys. Fluids*, 2015, **27**(1), 012103.
- 59 T. Dong, W. H. Weheliye, P. Chausset and P. Angeli, An experimental study on the drop/interface partial coalescence with surfactants, *Phys. Fluids*, 2017, **29**(10), 102101.
- 60 S. Shim and H. A. Stone, Damped coalescence cascade of liquid drops, *Phys. Rev. Fluids*, 2017, **2**(4), 044001.
- 61 K. Haldar, S. Chakraborty and S. Chakraborty, Influence of Marangoni stress on the variation in number of coalescence cascade stages, *Can. J. Chem. Eng.*, 2019, **97**(4), 983–994.
- 62 C. Berendsen, C. Kuijpers, J. Zeegers and A. Darhuber, Dielectrophoretic deformation of thin liquid films induced by surface charge patterns on dielectric substrates, *Soft Matter*, 2013, **9**(19), 4900–4910.
- 63 B. He and A. A. Darhuber, Electrical surface charge patterns induced by droplets sliding over polymer and photoresist surfaces, *J. Micromech. Microeng.*, 2019, **29**(10), 105002.

